

# Stochastic Modeling for Learnable Human Pose Triangulation

Kristijan Bartol, David Bojanić, Tomislav Petković, Tomislav Pribanić

University of Zagreb, Faculty of Electrical Engineering and Computing

Department of Electronic Systems and Information Processing

kristijan.bartol@fer.hr

## Abstract

We propose a stochastic modeling framework for 3D human pose triangulation and evaluate its performance across different datasets and spatial camera arrangements. The common approach to 3D pose estimation is to first detect 2D keypoints in images and then apply the triangulation from multiple views. However, the majority of existing triangulation models are limited to a single dataset, i.e. camera arrangement and their number. Moreover, they require known camera parameters. The proposed stochastic pose triangulation model successfully generalizes to different camera arrangements and between two public datasets. In each step, we generate a set of 3D pose hypotheses obtained by triangulation from a random subset of views. The hypotheses are evaluated by a neural network and the expectation of the triangulation error is minimized. The key novelty is that the network learns to evaluate the poses without taking into account the spatial camera arrangement, thus improving generalization. Additionally, we demonstrate that the proposed stochastic framework can also be used for fundamental matrix estimation, showing promising results towards relative camera pose estimation from noisy keypoint correspondences.

## Introduction

Human pose estimation finds the locations of the keypoints that represent a subset of human joints. It is a very active computer vision research area, especially due to the advances in deep learning. Pose estimation is particularly important for applications such as medicine, fashion industry, anthropometry, and entertainment (Bartol et al. 2021). In this work, we focus on 3D human pose estimation from multiple views in a single time frame.

The common approach to multi-view pose estimation is to (1) detect 2D keypoints in each view using pretrained pose detector (Xiao, Wu, and Wei 2018), and then (2) triangulate. The naive approach simply takes 2D detections as they are and applies triangulation from all available views. This simple approach is surprisingly effective, achieving close-to-state-of-the-art performance, as shown in the Experiments. However, the naive approach depends solely on the performance of the 2D detector. Due to the variety of poses and self-occlusions, some views contain erroneous de-

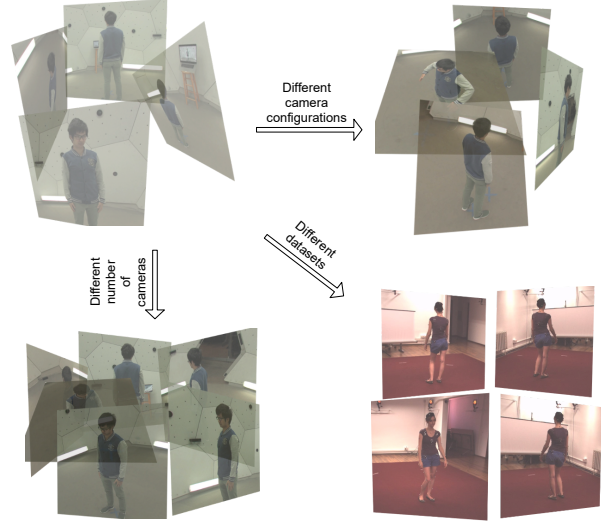


Figure 1: We propose a stochastic framework for human pose triangulation from multiple views and demonstrate its generalization performance across different relative camera placement, number of cameras, and datasets. The upper two and the lower left image shows different camera placements and their number on Panoptic Studio dataset (Joo et al. 2017). The lower right part shows the Human3.6M's 4-camera arrangement (Ionescu et al. 2014).

tectors, which should be ignored or their influence mitigated in the triangulation process. One way to ignore the erroneous detections is to apply RANSAC, marking the keypoints whose reprojection errors are above a threshold as outliers (Simon et al. 2017; He et al. 2020). The problem with vanilla RANSAC is that it is non-differentiable, so the gradients are not back-propagated, which disables end-to-end learning. Most of the state-of-the-art 3D pose estimation approaches extract 2D image features such as heatmaps and combine them for 3D elevation in an end-to-end fashion (Iskakov et al. 2019; Remelli et al. 2020; Qiu et al. 2019); we refer to those approaches as the *learnable triangulation approaches*.

Due to mostly-fixed set of cameras during training, the learnable triangulation approaches are often bounded to a single camera arrangement and their number. Several works attempt to generalize outside the training data (Remelli et al.

2020; Iskakov et al. 2019), but the demonstrated performance on novel views is significantly lower than using the base views.

Inspired by stochastic learning (Schulman et al. 2015) and its applications in computer vision (Brachmann et al. 2017; Brachmann and Rother 2018), we propose *stochastic modeling* for human pose triangulation. First, we generate a pool of random hypotheses. A hypothesis is a 3D pose where the points are obtained by triangulation of a random subset of views for each joint separately. Each generated hypothesis is passed through a scoring neural network. The loss function is an expectation of the triangulation error, i.e.  $\mathbb{E}(h_i) = \sum_i e_i s_i$ , where  $e_i$  is the error for the hypothesis  $h_i$  and  $s_i$  is the respective score. By minimizing the error expectation, the model learns the distribution of hypotheses. The key idea is to learn to evaluate 3D pose hypotheses without taking into account the spatial camera arrangement used for triangulation.

The proposed approach has several practical advantages over the previous methods. First, we demonstrate the successful generalization on two public datasets and different relative camera placements. The scoring network only uses normalized 3D poses and thus is invariant to relative camera poses. Second, given that the scoring network takes whole 3D poses as input, it learns a human pose prior.

We demonstrate consistent performance across two public datasets, Human3.6M (Ionescu et al. 2014) and Panoptic Studio (Joo et al. 2017). Compared to (Iskakov et al. 2019) and (Remelli et al. 2020), we report improved generalization performance between the datasets and across different camera placements, respectively. Finally, we apply the same stochastic modeling framework to the problem of fundamental matrix estimation from noisy 2D detections and compare it to the standard 8-point algorithm, showing that the proposed framework can be successfully applied to computer vision problems other than human pose triangulation.

## Related Work

We distinguish two types of related work. First, we focus on 3D pose estimation methods that apply triangulation or attempt to generalize between the different view combinations and datasets. Second, we relate to keypoint correspondence methods and point out how our problem differs from the standard correspondence problem.

**Triangulation.** Most of the single-person approaches either use robust triangulation (RANSAC) or apply learnable triangulation. Several methods (Kocabas, Karagoz, and Akbas 2019; Simon et al. 2017; Moon et al. 2020) based on robust triangulation use RANSAC on many (more than four) views to apply triangulation only on inlier detection candidates to produce pseudo ground truth data. (He et al. 2020) exploits epipolar constraints to find the keypoint matches between multiple images and then applies robust triangulation.

The standard approach for learnable (differentiable) triangulation approaches is to first extract 2D pose heatmaps, where each heatmap represents the probability of a keypoint location. Cross-view fusion (Qiu et al. 2019) builds upon the pictorial structures model (Belagiannis et al. 2014) to

combine 2D keypoint features from multiple views to estimate a 3D pose. An algebraic triangulation (Iskakov et al. 2019) estimate the confidence for each keypoint detection and applies weighted triangulation. Their volumetric approach combines the multi-view features and build the volumetric grid, obtaining the current state-of-the-art for single-frame 3D pose. Finally, (Remelli et al. 2020) fuses the features into a unified latent representation that is less memory intensive than the volumetric grids. Similar to us, they also attempt to disentangle from the specific spatial camera arrangement.

**Keypoint correspondence.** The standard keypoint-based computer vision approaches, such as structure-from-motion (Schönberger and Frahm 2016), rely on sparse keypoint detections to establish initial 3D geometry. The core problem is to determine the correspondences between the extracted keypoint detections across images, under various illumination changes, texture-less surfaces, and repetitive structures (Furukawa and Hernández 2015). The usual approach is to apply keypoint descriptor such as SIFT (Lowe 2004) and find inlier correspondences using RANSAC (Fischler and Bolles 1981). Even though this paradigm is successful in practice, it is not differentiable and, therefore, cannot be used in an end-to-end learning.

Several works have proposed differentiable RANSAC (DSAC) (Brachmann et al. 2017) or its soft alternatives. The successful soft RANSAC alternative (Yi et al. 2018) learns to extract both local features of each data point, as well as retain the global information of the 3D scene. Similar to us, they also convincing generalization capabilities to unseen 3D scenes. On the other hand, DSAC and its variants (Brachmann and Rother 2018, 2019) propose a differentiable version of RANSAC using a probabilistic learning scheme, i.e. minimizing the error expectation. We follow their approach, but also discover that different strategies work better for our problem.

In contrast to the standard keypoint matching approaches, we extract keypoints with already known human joint correspondences between the views. However, our correspondent keypoints are noisy, oscillating around the centers of the joints, which potentially leads to erroneous triangulation. Our focus is, therefore, to achieve robustness to noise instead of robustness to outliers. To the best of our knowledge, we are the first to explicitly investigate noise-free human pose triangulation using stochastic learning.

## Method

We first describe the generic stochastic framework, and then describe it more specifically for pose triangulation and fundamental matrix estimation. The framework consists of several steps, shown in Fig. 2:

1. **Pre-training.** Prior to stochastic learning, the 2D poses (keypoints) are extracted for all images in the dataset. In all our experiments, we use the keypoints extracted using a baseline model (Xiao, Wu, and Wei 2018) pretrained on Human3.6M dataset. The input to stochastic model, therefore, consists of keypoint detections,  $\mathbf{y}_{ijk} \in \mathbf{Y}$ , where  $i \in \{1, 2, \dots, T\}$  is a frame index,  $j \in \{1, 2, \dots, V\}$

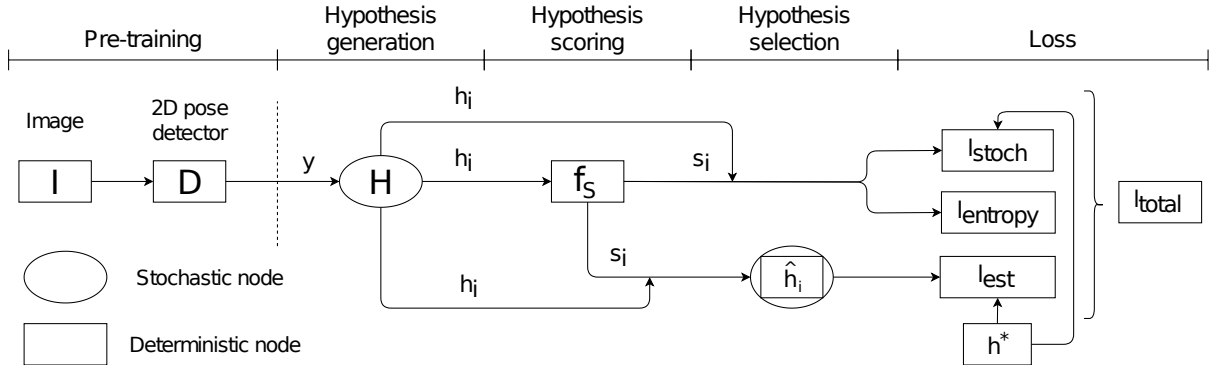


Figure 2: An overview of our method. Before stochastic learning, 2D keypoints,  $y$  are extracted. In each frame, the hypothesis pool,  $h_i \in H$ , is generated, and the poses are passed through the scoring network,  $f_S$ . Based on the estimated scores  $s_i$ , two hypothesis selection strategies, stochastic and deterministic (weighted), are applied, producing  $h_{stoch}$ , i.e.  $h_{weight}$ . Finally, the total loss,  $l_{total}$ , consists of two ( $l_{stoch}$ ,  $l_{entropy}$ ) or three ( $l_{weight}$ ) components.

is a view (camera) index, and  $k \in \{1, 2, \dots, J\}$  is a joint (body keypoint) index.

2. **Hypothesis generation,  $H$ .** As it is possible to generate extremely large number of hypotheses, only a subset of random hypotheses is created. Following (Schulman et al. 2015) and (Brachmann et al. 2017), we model the hypothesis generation step as a *stochastic* node.
3. **Hypothesis scoring,  $f_S$ .** Each generated hypothesis  $h_i \in H$  is scored using a scoring function,  $f_S(h_i, y_i) = s_i$ . The scoring function is a neural network, i.e. a multi-layer perceptron. The network architectures for 3D pose triangulation and fundamental matrix estimation differ and are specified at the end of the Experiments. The network is the only learnable part of our model. The estimated scores  $s_i$ , passed through the Gumbel-Softmax,  $\sigma_{GS}(s_i)$  (Eq. 2), represent the estimated probability distribution,  $\theta$ .
4. **Hypothesis selection,  $\hat{h}_i$ .** In training time, we select hypothesis as the weighted average of all generated hypotheses (deterministic selection):

$$\hat{h}_{weight} = \sum_i s_i h_i, \quad h_i \in H, \quad (1)$$

where the scores  $s_i$  are used as weights. In inference, we experiment with different selection strategies (both deterministic and stochastic) as described in the Experiments.

5. **Loss calculation,  $l_{total}$ .** The loss function consists of several components:
  - (a) Stochastic loss. Following (Brachmann et al. 2017), we calculate our stochastic loss as an expectation of error for all hypotheses,  $l_{stoch} = \mathbb{E}(h_i) = \sum_i e_i(h_i, h^*) s_i$ , where  $e_i$  is the error of the estimated hypothesis with respect to the ground truth,  $h^*$ , and  $s_i$  represent the probability that the error is minimal.
  - (b) Entropy loss. Score estimations tend to quickly converge to zero. To stabilize the estimation values, we follow (Brachmann and Rother 2018) and minimize an entropy function,  $l_{entropy} = -\sum_i s_i \log(s_i)$ .

- (c) Estimation loss. The estimation loss is the error of the selected hypothesis,  $l_{est} = e_i(\hat{h}_i, h^*)$ . We notice significant improvement of the hypothesis estimation performance when this loss component is included.

Finally, the total loss is a sum of the three components,  $l_{total} = \alpha l_{stoch} + \beta l_{entropy} + \gamma l_{weight}$ , where  $\alpha$ ,  $\beta$ , and  $\gamma$  are fixed hyperparameters that regulate relative values between the components.

In order for the estimated scores  $s_i$  to represent the probabilities, their values need to be normalized into  $[0, 1]$  range. The standard way to normalize the output values is to apply the softmax function,  $\sigma(s_i) = \frac{\exp s_i}{\sum_j \exp s_j}$ . To avoid early convergence, we use the Gumbel-Softmax function (Jang, Gu, and Poole 2017; Maddison, Mnih, and Teh 2017):

$$\sigma_{GS}(s_i) = \frac{\exp((\log s_i + g_i)/\tau)}{\sum_{j=1}^k \exp((\log s_j + g_j)/\tau)}, \quad (2)$$

where  $\tau$  is a temperature parameter, and  $g_i$  represent samples drawn from *Gumbel*(0, 1) (Maddison, Tarlow, and Minka 2014) distribution. The temperature  $\tau$  regulates the broadness of the distribution. For lower temperatures ( $\tau < 1$ ), the influence of lower-score hypotheses is limited compared higher-score hypotheses, and vice versa. We achieve the best results by starting with higher temperature and lowering it over time. The purpose of *Gumbel*(0, 1) is to add noise to each distribution, while retaining its statistical properties, which allows the model to be more flexible with the hypothesis selection.

### Learnable Pose Triangulation

We now describe the stochastic framework specifically for learning human pose triangulation. The 3D human pose hypothesis,  $h_i \in H$ , is generated in the following way. For each joint  $k$ , a subset of views,  $v_k$ , is randomly selected. The detections from the selected views are triangulated to produce a 3D joint.

The input to the pose scoring network,  $f_{S,pose}$  are 3D pose coordinates,  $p$ , normalized in the following way: we select

three points: left and right shoulder and the pelvis (between the hips), calculate the rotation between their normal, and the normal of the  $xy$ -plane, and apply that rotation to all coordinates. Other than the 3D pose coordinates, we also extract body part lengths. Finally, we concatenate both normalized 3D coordinates and the body part lengths into a 1D vector and pass it through the network. The output is a scalar,  $s_i$ , representing the score of the hypothesis  $h_i$ .

The pose estimation error,  $e_i(\hat{h}_i, h^*)$ , is a mean per-joint precision error (MPJPE) (Ionescu et al. 2014) between the estimated 3D pose,  $\hat{\mathbf{p}}_i$ , and the ground truth,  $\mathbf{p}^*$ :

$$e_i(\hat{h}_i, h^*) = e_i(\hat{\mathbf{p}}_i, \mathbf{p}^*) = \frac{1}{J} \sum_k^J \|\hat{p}_{ik} - p_k^*\|_2, \quad (3)$$

where  $p_{ik}$  is the  $k$ -th keypoint of the  $i$ -th pose.

## Learnable Fundamental Matrix Estimation

We describe how to learn fundamental matrix estimation between the pairs of cameras using the proposed stochastic framework. The fundamental matrix describes the relationship between the two views via  $x_1 F x_2^\top = 0$ , where  $x_1$  and  $x_2$  are the corresponding 2D points in the first (reference) and the second (target) view. From the fundamental matrix, relative rotation and translation (the relative camera pose) between the views can be obtained (Hartley and Zisserman 2003).

The relative camera pose hypothesis,  $h_i$ , is generated in a slightly different way than the 3D pose hypothesis. The required number of points to determine the fundamental matrix is 8 when an 8-point algorithm is used (Longuet-Higgins 1987). However, with the presence of noise, the required number of points is usually much higher. Instead of using a single time frame as in pose triangulation, we select the keypoints from  $M$  frames, having a total of  $M * J$  individual point correspondences. The camera hypothesis  $h_i$  is obtained using a subset of  $T < M * J$  correspondences, passed through an 8-point algorithm. The result of an 8-point algorithm are four possible rotations and translations, which we resolve in a standard way (Hartley and Zisserman 2003).

The input to the camera pose scoring network,  $f_{S, cam}$ , are the distances between the corresponding back-projected lines, obtained using the reference camera parameters,  $(R_{ref}, t_{ref})$ , and the estimated relative camera pose,  $(R_{rel,i}, t_{rel,i})$ . The idea is that the raw point correspondences do not contain enough information for the model to evaluate the hypothesis. To achieve the permutation invariance between the line distances on the input, we sort the values before passing it through the network.

The camera pose hypothesis,  $\hat{h}_{weight}$ , is selected as the weighted average of the rotation<sup>1</sup>, i.e. the translation of all hypotheses. The hypothesis estimation error,  $e_i$ , is calculated as:

$$e_i(\hat{h}_i, h^*) = e_i(\hat{\mathbf{X}}_i, \mathbf{X}^*) = \|\hat{\mathbf{X}}_i - \mathbf{X}^*\|_2 \quad (4)$$

<sup>1</sup>The rotations are converted to quaternions, for simplicity.

where  $\mathbf{X}^*$  are random 3D points (used as ground truth), and  $\hat{\mathbf{X}}_i$  are 3D points obtained by projecting the points  $\mathbf{X}^*$  to 2D planes, using the estimated parameters,  $(\hat{R}_i, \hat{t}_i)$ , and then projected back to 3D. More specifically, using the estimated, target projection matrix,  $\hat{P}_i = K_i[\hat{R}_i|\hat{t}_i]$  and the reference projection matrix,  $P_{ref} = K_{ref}[R_{ref}|t_{ref}]$ , the points  $\mathbf{X}^*$  are first projected to 2D,  $\hat{\mathbf{x}}_i = \hat{P}_i \mathbf{X}^*$ , and then triangulated using  $P_{ref}$  and  $\hat{P}_i$ . The intrinsic matrices  $K_i$  are assumed to be known for all cameras.

## Experiments

The stochastic framework is evaluated on Human3.6M (Ionescu et al. 2014) and Panoptic Studio (Joo et al. 2017) datasets. As most of the previous 3D pose estimation approaches presented their results on Human3.6M, we use it for the quantitative comparison to state-of-the-art. Panoptic Studio contains relatively large number of cameras (31) with useful data annotations (camera parameters, 3D and 2D poses). We use the Panoptic Studio dataset to evaluate the generalization performance between different camera arrangements and their number. We also evaluate the generalization between the Panoptic Studio and Human3.6M datasets. As experiments are based on a single-person pose estimation, we use Panoptic Studio sequences that contain single person in the scene (Xiang, Joo, and Sheikh 2019).

Other than the evaluation of our best result ( $\hat{h}_{weight}$ ), we also compare between different hypotheses:

- Weighted average hypothesis,  $\hat{h}_{weight}$ ,
- Average hypothesis,  $\hat{h}_{avg}$ , obtained as an average of all hypotheses,
- Most probable hypothesis,  $\hat{h}_{most}$ , the hypothesis with maximal estimated score,  $s_{max}$ ,
- Least probable hypothesis,  $\hat{h}_{least}$ , the hypothesis with minimal estimated score,  $s_{min}$ ,
- Stochastic hypothesis,  $\hat{h}_{stoch}$ , selected randomly, based on the estimated distribution  $\theta$ ,
- Random hypothesis,  $\hat{h}_{stoch}$ , selected randomly from an uniform distribution,
- Best hypothesis<sup>1</sup>,  $h_{best}$ , with the lowest error,  $e_{min}$ , and
- Worst hypothesis<sup>1</sup>,  $h_{worst}$ , the hypothesis with the highest error,  $e_{max}$  when evaluated against the ground truth.

Additionally, we also compare ourselves with two more results - the hypothesis obtained using the naive triangulation, and RANSAC as reported in (Iskakov et al. 2019). The purpose of those hypotheses is to show the variety of the pose distribution and their properties.

## Overall Performance

The comparison to state-of-the-art is shown in Tab. 1. Compared to the best-performing single-frame method, we obtain 8.3 mm worse MPJPE, but compared to the majority of other recent methods, we are significantly better.

<sup>1</sup>Note that these hypotheses are not available in inference, but we use it to show the performance of the best and worst single hypothesis in the hypothesis pools.

Table 1: Quantitative comparison to state-of-the-art on Human3.6M dataset, per actions. All values are showing MPJPE scores (mm).

Protocol I, abs. positions	Dir.	Disc.	Eat	Greet	Phone	Photo	Pose	Purch.	Sit	SitD.	Smoke	Wait	WalkD.	Walk	WalkT.	Avg
Tome et al. (Tomè et al. 2018)	43.3	49.6	42.0	48.8	51.1	64.3	40.3	43.3	66.0	95.2	50.2	52.2	51.1	43.9	45.3	52.8
(Kadkhodamohammadi and Padoy 2021)	39.4	46.9	41.0	42.7	53.6	54.8	41.4	50.0	59.9	78.8	49.8	46.2	51.1	40.5	41.0	49.1
Cross-view fusion (Qiu et al. 2019)	28.9	32.5	26.6	28.1	28.3	29.3	28.0	36.8	41.0	30.5	35.6	30.0	28.3	30.0	30.5	31.2
Epipolar transformers (He et al. 2020)	25.7	27.7	23.7	24.8	26.9	31.4	24.9	26.5	28.8	31.7	28.2	26.4	23.6	28.3	23.5	26.9
Volumetric triang. (Iskakov et al. 2019)	18.8	20.0	19.3	18.7	20.2	19.3	18.7	22.3	23.3	29.1	21.2	20.3	19.3	21.6	19.8	<b>20.8</b>
Ours ( $h_{weight}$ )	27.5	28.4	29.3	27.5	30.1	28.1	27.9	30.8	32.9	32.5	30.8	29.4	28.5	30.5	30.1	29.1

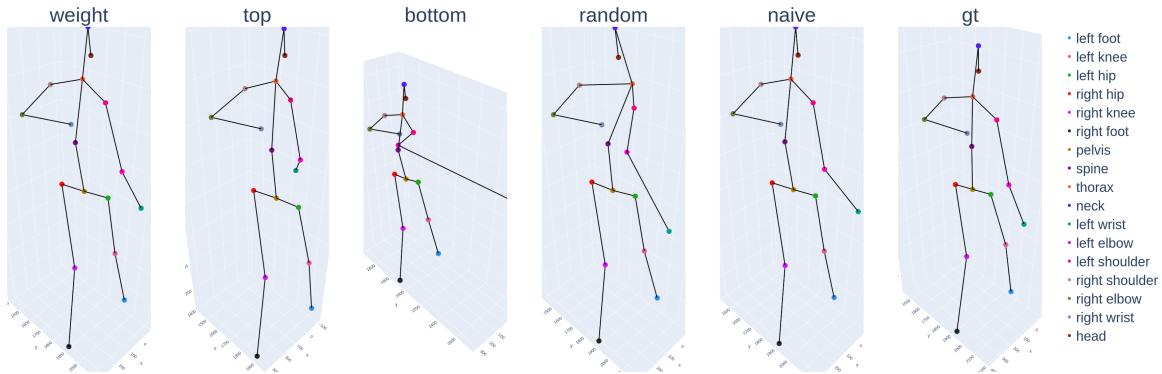


Figure 3: Qualitative comparison between five 3D pose hypotheses compared to ground truth, on Human3.6M.

Table 2: Overall quantitative comparison between the hypotheses. The values are showing MPJPE scores in mm (the lower is better).

Hypothesis	Human3.6M	Panoptic Studio
$\hat{h}_{weight}$	29.1	<b>24.9</b>
$\hat{h}_{avg}$	31.2 <b>+2.1</b>	25.9 <b>+1.0</b>
$\hat{h}_{most}$	41.3 <b>+12.2</b>	25.0 <b>+0.1</b>
$\hat{h}_{least}$	74.5 <b>+45.4</b>	29.8 <b>+3.9</b>
$\hat{h}_{stoch}$	41.3 <b>+12.2</b>	26.5 <b>+1.6</b>
$\hat{h}_{random}$	45.0 <b>+15.9</b>	26.1 <b>+1.2</b>
$\hat{h}_{best}$	22.3 -6.8	24.4 -0.5
$\hat{h}_{worst}$	98.9 +69.8	31.0 +6.1
$\hat{h}_{naive}$	27.9 <b>-1.2</b>	25.7 <b>+0.8</b>
RANSAC	<b>27.4</b> <b>-1.7</b>	39.5 <b>+14.6</b>

Table 2 shows the MPJPE scores of different pose hypotheses on the two datasets, as well as the hypothesis obtained using naive triangulation and the RANSAC result, reported in (Iskakov et al. 2019). Even though our weighted average hypothesis,  $\hat{h}_{weight}$ , is outperformed by naive and RANSAC approach on Human3.6M, we show an improvement on Panoptic Studio. Also note that the simple naive triangulation is significantly better on Human3.6M than most of the state-of-the-art results.

Regarding other results, the average hypothesis,  $\hat{h}_{avg}$  performs better than the stochastic,  $\hat{h}_{stoch}$ . The stochastic performs even worse than the random hypothesis on Panoptic Studio. The most probable hypothesis,  $\hat{h}_{most}$ , outperforms the average on Panoptic Studio. Note that the difference between best and worst hypothesis ( $\hat{h}_{best}$ ,  $\hat{h}_{worst}$ ) is significantly different on the two datasets. This suggests that the

hypotheses generated on Panoptic Studio are more similar to each other and the distribution is less broad. The difference between the most and the least probable hypothesis ( $\hat{h}_{most}$ ,  $\hat{h}_{least}$ ) is reasonable on both datasets, which confirms that our model learned to differentiate between the poses.

Fig. 3 shows the qualitative performance comparison between several hypotheses. The least probable and the random hypothesis ( $\hat{h}_{least}$ ,  $\hat{h}_{random}$ ) do not have visually plausible 3D reconstructions. The most probable hypothesis,  $\hat{h}_{most}$  have obvious reconstruction errors on right arm and shoulder. The weighted and the naive hypothesis ( $\hat{h}_{weight}$ ,  $\hat{h}_{naive}$ ) are comparable and close to ground truth. For more overall performance results, please see the Supplementary Appendix.

## Human Pose Prior

We demonstrate the successful pose prior learning of the pose scoring network,  $f_{S,pose}$ . Some previous works that attempt human pose prior learning (Drover et al. 2018; Xu et al. 2020; Belagiannis et al. 2014) use a similar approach to ours. The idea is to differentiate between the 3D poses that are more plausible with respect to several human body properties and vice versa. The properties that can be extracted from the 3D pose are based body part lengths and between-joint angles. In this work, we focus on body part lengths, i.e. *left-right body symmetry*.

The body symmetry is measured for six different body left-right part pairs: upper arms, lower arms, shoulders, hips, upper legs, and lower legs. For each pair,  $l$ , we calculate the ratio,  $r_{il}$  between the left and right part, in each time frame,  $i$ . The final pose prior metric is a variance of the ratios over time:

Table 3: The demonstration of the generalization performance (MPJPE in mm) on five data sets, featuring different spatial camera placements, different number of cameras, and different datasets (CMU Panoptic Studio and Human3.6M). Each row shows the performance on five test sets when the specified train set is used. The maximal difference between the scores for particular test sets is shown in the last column.

Train	CMU1		CMU2		CMU3		CMU4		H36M		Max diff.
Test	CMU1	25.8	CMU1	25.8	CMU1	25.6	CMU1	25.2	CMU1	25.6	2.3%
	CMU2	25.4	CMU2	26.0	CMU2	25.5	CMU2	25.6	CMU2	25.9	2.4%
	CMU3	24.9	CMU3	26.0	CMU3	25.0	CMU3	25.0	CMU3	25.7	4.4%
	CMU4	25.1	CMU4	25.6	CMU4	25.3	CMU4	25.1	CMU4	25.5	<b>2.0%</b>
	H36M	33.5	H36M	33.4	H36M	31.0	H36M	32.5	H36M	29.1	22.0%

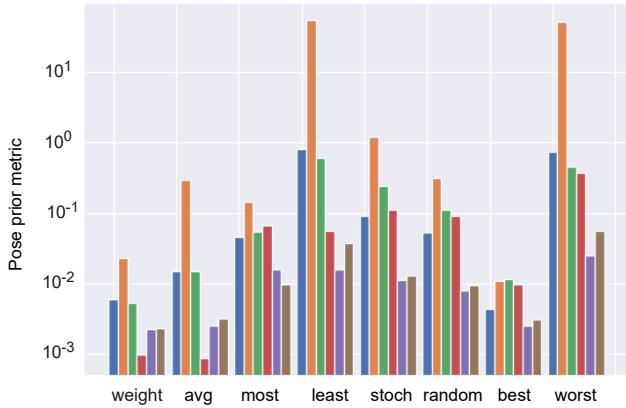


Figure 4: Evaluation of the human pose prior metric for different hypotheses, and six body part pairs (lower is better).

$$S^2 = \frac{\sum_i (r_{il} - \bar{r}_l)^2}{T}, \quad (5)$$

where  $\bar{r}_l$  is the mean ratio for the pair  $l$ , and  $T$  is the number of frames. The reason for using ratios instead of the differences between the body parts is that some people are naturally asymmetric, so the idea is only to measure the consistency over time.

Fig. 4 shows the pose prior metrics for the subject 9 of the Human3.6M dataset, for different hypotheses. As expected, the values are generally the lowest for our best performing hypothesis,  $\hat{h}_{\text{weight}}$ , followed by the average hypothesis,  $\hat{h}_{\text{avg}}$ . The difference between the most probable and the least probable hypothesis ( $\hat{h}_{\text{most}}, \hat{h}_{\text{least}}$ ) suggests that we successfully learned body pose prior, i.e. differentiate between the plausible poses with respect to the body symmetry consistency over time. Note that the best hypothesis,  $\hat{h}_{\text{best}}$ , is comparable to  $\hat{h}_{\text{weight}}$ .

## Generalization Performance

One of the most important properties of the proposed model is that it generalizes well to different spatial arrangement and number of cameras, and different datasets, which is a major limitation of the previous models. To evaluate the generalization performance across data sets, we select five different camera configurations:

1. Cameras 1, 2, 3, 4, 6, 7, 10 (CMU1),

2. Cameras 12, 16, 18, 19, 22, 23, 30 (CMU2),
3. Cameras 10, 12, 16, 18 (CMU3),
4. Cameras 6, 7, 10, 12, 16, 18, 19, 22, 23, 30 (CMU4), and
5. Cameras 0, 1, 2, 3 (H36M).

One of the five data sets is used for training and validation, and then used for testing on all five configurations. The camera sets CMU1 and CMU2 differ in camera arrangement, the sets CMU3 and CMU4 differ in both number of cameras and their arrangement, and the H36M set includes all four cameras on Human3.6M dataset.

Table 3 shows consistent performance on each of the five camera arrangements, i.e. datasets, regardless of the dataset used for training and validation. Note that this transfer learning property can be exploited both in training time and in inference. One is therefore able to combine different camera arrangements and datasets to extend its dataset, while still being able to generalize to unseen data.

Compared to 34 mm of (Iskakov et al. 2019), we achieve 31.0 mm MPJPE error, when generalizing from Panoptic Studio to Human3.6M. We also achieve significantly less degradation in generalization performance between the view arrangements than (Remelli et al. 2020). As we do not evaluate our performance on Total Capture dataset (Trumble et al. 2017), we compare ourselves in percentages. Our worst transfer learning drops in performance by 22% on Human3.6M test set (29.1 mm when learned on Human3.6M train set, and 35.5 mm when learned on CMU2), while the best transfer learning performance drop reported in (Remelli et al. 2020) is 39%. Between most of our selected camera configurations, we achieve insignificant drop in performance.

## Fundamental Matrix Estimation

Table 4 shows the fundamental matrix estimation results on all combinations of Human3.6M views on Human3.6M. The camera arrangement with respect to the specified indexes, is shown in Fig. 6. The four metrics are used for the evaluation:

- Rotation error,  $E_R = \|\text{quat}(\hat{R}_{\text{rel}}) - \text{quat}(R_{\text{rel}}^*)\|_1$ , where  $\text{quat}()$  represents the conversion to quaternions,
- Translation error (mm),  $E_t = \|\hat{t}_{\text{rel}} - t_{\text{rel}}^*\|_2$ ,
- 2D error (pixels),  $E_{2D} = \|\hat{\mathbf{x}}_i - \mathbf{x}^*\|_2$ , where  $\mathbf{x}^*$  represents random 3D points,  $\mathbf{X}^*$ , projected using the ground truth relative projection matrix,  $P^*$ , and
- 3D error (mm),  $E_{3D} = e_i(\hat{h}_i, h^*)$ , from Eq. 4.

Table 4: Evaluation of fundamental matrix estimation for all pairs of views on Human3.6M, based on four error metrics.

	$E_R$	$E_t$	$E_{2D}$	$E_{3D}$
(1, 2)	4.8e-3	<b>4.8e+0</b>	8.1e-1	<b>4.9e+0</b>
(1, 3)	1.7e-2	2.3e+1	3.7e+0	2.3e+1
(1, 4)	9.8e-3	2.7e+1	2.3e+0	1.3e+1
(2, 3)	<b>2.1e-3</b>	9.9e+0	<b>7.2e-1</b>	1.3e+1
(2, 4)	3.2e-2	4.9e+0	1.3e+0	2.3e+1
(3, 4)	4.7e-3	8.5e+0	1.2e+0	5.5e+0

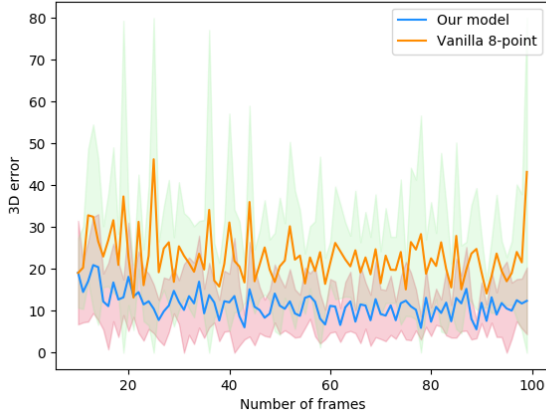


Figure 5: The comparison of the  $E_{3D}$  errors between the stochastic model and the 8-point algorithm, for different number of input frames (between 10 and 100), using the camera pair (2, 3) of Human3.6M. For every number of frames, the experiments is done 10 times. The lines show mean values, and the fill parts show standard deviations. The values are clipped to 80 mm.

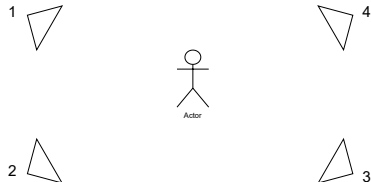


Figure 6: Human3.6M camera arrangement.

The obtained results show that the model achieves sub-pixel error ( $E_{2D}$ ) for two pairs of views ((1, 2) and (2, 3)), and only few pixels in the worst case, which corresponds to several millimeters when reprojected back to 3D ( $E_{3D}$ ). Note that the adjacent pairs of views have lower errors than the opposite pairs, as expected.

In Fig. 5, we compare our 3D errors ( $E_{3D}$ ) to the vanilla 8-point algorithm, on the (2, 3) camera pair, using different number of input frames. Our model consistently outperforms the 8-point algorithm, showing robustness to noise and increased confidence due to lower variance. For more fundamental matrix estimation results, please see the Supplementary Appendix.

Table 5: The Table of hyperparameters for the two tasks.

	3D pose	Camera
Learning rate	$5 * 10e^{-4}$	$10e^{-5}$
$\tau$	1.5	1.2
$\alpha, \beta, \gamma$	(1.0, 0.01, 0.02)	(1.0, 0.01, 0.0)
Network layer sizes	(1000, 900, 900, 900, 700)	(1000, 900, 900, 900)
# hypotheses in sample	200	100
Batch size	16	16

## Implementation Details

The selected hyperparameters set is shown in Tab. 5. The two hyperparameters used specifically for pose triangulation, i.e., fundamental matrix estimation, are the number of joints in the pose model,  $J = 17$ , and the number of frames from which the camera hypotheses are sampled,  $M = 80$ .

The required number of training iterations is relatively small. We obtain our best results using only 500 iterations. In each iteration, we generate 200 hypotheses. This is a great advantage of the approach, especially when only small amount data annotations are available. Moreover, the training time is shorter, which simplifies the optimal hyperparameter search. Finally, the current implementation fits into  $\sim 1\text{GB}$  of GPU memory. However, this would increase if the images are used during training. We comment on the hyperparameter selection in detail in the Supplementary Appendix.

## Conclusion

The proposed stochastic framework is a promising novel directions for 3D human pose estimation, as well as other related computer vision problems, such as camera pose estimation. Compared to previous stochastic learning approaches (Brachmann et al. 2017; Brachmann and Rother 2018), we apply it to achieve robustness to noise, instead of robustness to outliers. The demonstrated results show convincing generalization capabilities between different camera arrangements and datasets, which has not been shown before. Note that the model requires relatively little training data, which makes the training faster and more convenient for the smaller datasets.

The overall performance is competitive in both pose triangulation and camera pose estimation tasks. The reasonable next step is to use the image features for an end-to-end learning, which should further improve the performance and come closer to the state-of-the-art. We argue that the future model will retain its generalization capabilities when learned end-to-end, as the scoring network is invariant to the input data configuration. The current model supports only a single-person pose triangulation. To extend to multi-person, we need to solve the keypoint correspondence problem between the people.

## References

Bartol, K.; Bojanic, D.; Petkovic, T.; and Pribanic, T. 2021. A Review of Body Measurement Using 3D Scanning. *IEEE Access*, 9: 67281–67301.

Belagiannis, V.; Amin, S.; Andriluka, M.; Schiele, B.; Navab, N.; and Ilic, S. 2014. 3D Pictorial Structures for Multiple Human Pose Estimation. In *2014 IEEE Conference on Computer Vision and Pattern Recognition*, 1669–1676.

Brachmann, E.; Krull, A.; Nowozin, S.; Shotton, J.; Michel, F.; Gumhold, S.; and Rother, C. 2017. DSAC — Differentiable RANSAC for Camera Localization. *2017 IEEE Conference on Computer Vision and Pattern Recognition (CVPR)*, 2492–2500.

Brachmann, E.; and Rother, C. 2018. Learning Less is More - 6D Camera Localization via 3D Surface Regression. *2018 IEEE/CVF Conference on Computer Vision and Pattern Recognition*, 4654–4662.

Brachmann, E.; and Rother, C. 2019. Neural-Guided RANSAC: Learning Where to Sample Model Hypotheses. *2019 IEEE/CVF International Conference on Computer Vision (ICCV)*, 4321–4330.

Drover, D.; Rohith, M.; Chen, C.-H.; Agrawal, A.; Tyagi, A.; and Huynh, C. P. 2018. Can 3D Pose be Learned from 2D Projections Alone? In *ECCV Workshops*.

Fischler, M. A.; and Bolles, R. C. 1981. Random Sample Consensus: A Paradigm for Model Fitting with Applications to Image Analysis and Automated Cartography. *Commun. ACM*, 24(6): 381–395.

Furukawa, Y.; and Hernández, C. 2015.

Hartley, R.; and Zisserman, A. 2003. *Multiple View Geometry in Computer Vision*. USA: Cambridge University Press, 2 edition. ISBN 0521540518.

He, Y.; Yan, R.; Fragkiadaki, K.; and Yu, S.-I. 2020. Epipolar Transformers. *2020 IEEE/CVF Conference on Computer Vision and Pattern Recognition (CVPR)*, 7776–7785.

Ionescu, C.; Papava, D.; Olaru, V.; and Sminchisescu, C. 2014. Human3.6M: Large Scale Datasets and Predictive Methods for 3D Human Sensing in Natural Environments. *IEEE Transactions on Pattern Analysis and Machine Intelligence*, 36(7): 1325–1339.

Iskakov, K.; Burkov, E.; Lempitsky, V.; and Malkov, Y. 2019. Learnable Triangulation of Human Pose. *2019 IEEE/CVF International Conference on Computer Vision (ICCV)*, 7717–7726.

Jang, E.; Gu, S.; and Poole, B. 2017. Categorical Reparameterization with Gumbel-Softmax. *ArXiv*, abs/1611.01144.

Joo, H.; Simon, T.; Li, X.; Liu, H.; Tan, L.; Gui, L.; Banerjee, S.; Godisart, T. S.; Nabbe, B.; Matthews, I.; Kanade, T.; Nobuhara, S.; and Sheikh, Y. 2017. Panoptic Studio: A Massively Multiview System for Social Interaction Capture. *IEEE Transactions on Pattern Analysis and Machine Intelligence*.

Kadkhodamohammadi, A.; and Padoy, N. 2021. A generalizable approach for multi-view 3D human pose regression. *Mach. Vis. Appl.*, 32: 6.

Kocabas, M.; Karagoz, S.; and Akbas, E. 2019. Self-Supervised Learning of 3D Human Pose Using Multi-View Geometry. *2019 IEEE/CVF Conference on Computer Vision and Pattern Recognition (CVPR)*, 1077–1086.

Longuet-Higgins, H. 1987. A computer algorithm for reconstructing a scene from two projections. In Fischler, M. A.; and Firschein, O., eds., *Readings in Computer Vision*, 61–62. San Francisco (CA): Morgan Kaufmann. ISBN 978-0-08-051581-6.

Lowe, D. G. 2004. Distinctive Image Features from Scale-Invariant Keypoints. *Int. J. Comput. Vision*, 60(2): 91–110.

Maddison, C. J.; Mnih, A.; and Teh, Y. 2017. The Concrete Distribution: A Continuous Relaxation of Discrete Random Variables. *ArXiv*, abs/1611.00712.

Maddison, C. J.; Tarlow, D.; and Minka, T. 2014. A\* Sampling. In *NIPS*.

Moon, G.; Yu, S.-I.; Wen, H.; Shiratori, T.; and Lee, K. M. 2020. InterHand2.6M: A Dataset and Baseline for 3D Interacting Hand Pose Estimation from a Single RGB Image. *ArXiv*, abs/2008.09309.

Qiu, H.; Wang, C.; Wang, J.; Wang, N.; and Zeng, W. 2019. Cross View Fusion for 3D Human Pose Estimation. *2019 IEEE/CVF International Conference on Computer Vision (ICCV)*, 4341–4350.

Remelli, E.; Han, S.; Honari, S.; Fua, P.; and Wang, R. Y. 2020. Lightweight Multi-View 3D Pose Estimation Through Camera-Disentangled Representation. *2020 IEEE/CVF Conference on Computer Vision and Pattern Recognition (CVPR)*, 6039–6048.

Schulman, J.; Heess, N.; Weber, T.; and Abbeel, P. 2015. Gradient Estimation Using Stochastic Computation Graphs. In *NIPS*.

Schönberger, J. L.; and Frahm, J.-M. 2016. Structure-from-Motion Revisited. In *2016 IEEE Conference on Computer Vision and Pattern Recognition (CVPR)*, 4104–4113.

Simon, T.; Joo, H.; Matthews, I.; and Sheikh, Y. 2017. Hand Keypoint Detection in Single Images Using Multiview Bootstrapping. *2017 IEEE Conference on Computer Vision and Pattern Recognition (CVPR)*, 4645–4653.

Tomè, D.; Toso, M.; Agapito, L.; and Russell, C. 2018. Rethinking Pose in 3D: Multi-stage Refinement and Recovery for Markerless Motion Capture. *2018 International Conference on 3D Vision (3DV)*, 474–483.

Trumble, M.; Gilbert, A.; Malleson, C.; Hilton, A.; and Collomosse, J. 2017. Total Capture: 3D Human Pose Estimation Fusing Video and Inertial Sensors. In *2017 British Machine Vision Conference (BMVC)*.

Xiang, D.; Joo, H.; and Sheikh, Y. 2019. Monocular Total Capture: Posing Face, Body, and Hands in the Wild. *2019 IEEE/CVF Conference on Computer Vision and Pattern Recognition (CVPR)*, 10957–10966.

Xiao, B.; Wu, H.; and Wei, Y. 2018. Simple Baselines for Human Pose Estimation and Tracking. In *ECCV*.

Xu, J.; Yu, Z.; Ni, B.; Yang, J.; Yang, X.; and Zhang, W. 2020. Deep Kinematics Analysis for Monocular 3D Human Pose Estimation. In *Proceedings of the IEEE/CVF Conference on Computer Vision and Pattern Recognition (CVPR)*.

Yi, K. M.; Trulls, E.; Ono, Y.; Lepetit, V.; Salzmann, M.; and Fua, P. 2018. Learning to Find Good Correspondences. *2018 IEEE/CVF Conference on Computer Vision and Pattern Recognition*, 2666–2674.